Pergamon

Int. J. Heat Mass Transfer. Vol. 40, No. 2, pp. 295–309, 1997

0017–9310/97 $15.00+0.00

PII: S0017-9310(96)00107-X

Solidification phenomena in picoliter size solder droplet deposition on a composite substrate

J. M. WALDVOGEL† and D. POULIKAKOS‡

Mechanical Engineering Department, University of Illinois at Chicago, 842 W. Taylor Street, Chicago, IL 60680, U.S.A.

(*Received* 8 *December* 1995 *and in final form* 16 *March* 1996)

Abstract—A predominantly theoretical study is presented of the impact and solidification of molten solder droplets on a multi-layer substrate. This problem is of central importance to the novel micromanufacturing process called solder jetting, in which picoliter-size solder droplets are dispensed for the attachment of microelectronic components. The theoretical model is based on a Lagrangian formulation, and accounts for a host of thermal-fluid phenomena, including surface tension and heat transfer with solidification. Deforming finite elements with integrated automatic mesh generation are utilized to accommodate the large deformations which develop during the computations. An experimental investigation is also presented in which deposits produced by a prototype solder jetting apparatus are analysed using scanning electron microscopy. Results of simulations are presented in which variations of the initial droplet temperature, impact velocity, thermal contact resistance and initial substrate temperature are studied to demonstrate their impact on droplet spreading, on final deposit shapes and on the times to initiate and complete freezing. In many cases, non-intuitive results are observed, such as the non-monotonic dependence of the solidification time on variations of many of the parameters considered. Detailed study of the final solidified shapes, as well as the droplet configuration and flow filed at the onset of phase change, indicate strong coupling between the droplet dynamics and the freezing behavior. Copyright © 1996 Elsevier Science Ltd.

1. INTRODUCTION

A novel micromanufacturing process, referred to as solder jetting, has been developed to dispense picoliter quantities of solder for the mounting of microelectronic components [1]. With this process, molten droplets are applied directly to the bonding pads of a semiconductor die (or chip) using a technique similar to ink-on-demand for ink-jet printing [1]. Solidified droplets (also called bumps) are then used in the flip–chip process to bond the die to a substrate or circuit board. In the flip–chip approach, the active surface of a chip is placed in contact with a pre-deposited array of solder droplets on the substrate, then the assembly is bonded in a reflow soldering oven.

A simplified schematic of a drop-on-demand solder jet device is provided in Fig. 1. In operation a voltage pulse is applied to produce a single 25–100 μm droplet, which is deposited on a substrate situated below. As shown, the substrate can be heated to modify the cooling rate of the impacting droplet. Partially flattened solder bump arrays have been printed onto a substrate in the laboratory using a prototype apparatus [1]. The shape of the solder deposit is affected by the dynamics of impact, as well as the heat removal process from the droplet to the substrate. How precisely the final solder bump shape can be predicted is crucial for the application of this technology to microelectronic packaging.

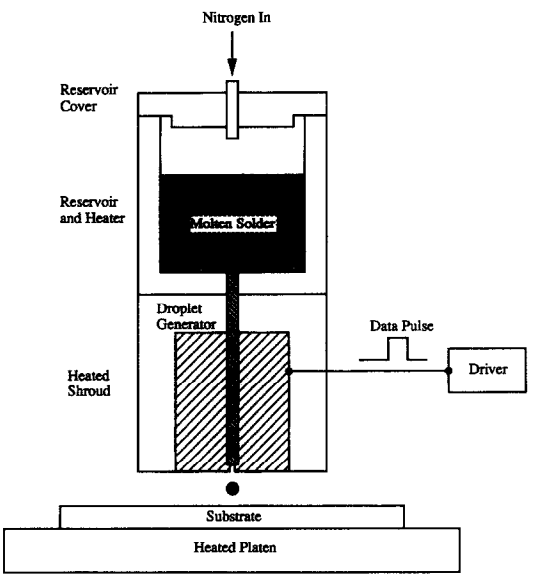

Fig. 1. Schematic of solder jet apparatus and substrate.

† Present address: Motorola Inc., Schaumburg, Illinois, 60196, U.S.A.

‡ Institute of Energy Technology, Swiss Federal Institute of Technology, ETH Center, Sonneggstrasse 3, Zurich, Switzerland. Author to whom correspondence should be addressed.

NOMENCLATURE

c	speed of sound [m s^{-1}]
C	dimensionless heat capacity
c_p	specific heat [J kg^{-1} K^{-1}]
d_0	initial diameter of droplet [m]
Fr	Froude number
g	gravitational acceleration [m s^{-2}]
h	heat transfer coefficient [W m^{-2} K^{-1}]
$\bar{h}$	dimensionless heat transfer coefficient
H	mean surface curvature [m^{-1}]
$\bar{H}$	dimensionless mean surface curvature
J	Jacobian
k	thermal conductivity [W m^{-1} K^{-1}]
K	dimensionless thermal conductivity
l_c	arbitrary layer thickness [m]
L	latent heat of fusion [J kg^{-1}]
L_c	dimensionless arbitrary layer thickness
M	Mach number
n	outward normal vector
$\hat{n}$	outward unit normal vector
p	droplet fluid pressure [N m^{-2}]
P	dimensionless droplet fluid pressure
Pr	Prandtl number
r	radial coordinate [m]
R	dimensionless radial coordinate
Re	Reynolds number
s	arc length along free surface
SHP	superheat parameter
Ste	Stefan number
t	time [s]
T	temperature [K]
u	radial velocity [m s^{-1}]
U	dimensionless radial velocity
v	axial velocity [m s^{-1}]
v_0	droplet impact velocity [m s^{-1}]
V	dimensionless axial velocity
w_i	Gauss weight
We	Weber number
z	axial coordinate [m]
Z	dimensionless axial coordinate
Z_c	dimensionless z-axis contact point
$Z_{r,2}$	dimensionless height of second surface ripple.

Greek symbols

α	thermal diffusivity [m^2 s^{-1}]
α_s	solid fraction
γ	surface tension coefficient [N m^{-1}]
θ	azimuthal coordinate
Θ	dimensionless temperature
κ	curvature
μ	viscosity [kg s^{-1} m^{-1}]
ρ	density [kg m^{-3}]
σ	stress [N m^{-2}]
$\bar{\sigma}$	dimensionless stress
τ	dimensionless time.

Subscripts

0	initial
1	droplet
2	substrate
c	contact
l	liquid
m	at equilibrium phase transition temperature
r	radial direction
R	dimensionless radial direction
s	solid
z	axial direction
Z	dimensionless axial direction
θ	azimuthal direction
Θ	dimensionless azimuthal direction.

In the theoretical model considered for this study, a molten metal droplet originally spherical in shape moves in the gravitational direction towards a horizontal, flat, multi-layer, composite substrate. The droplet velocity and diameter prior to impact are represented by v_0 and d_0, respectively. Typical values for these process parameters for solder jetting are 1.5 m s^{-1} and 50 μm. As the droplet impacts the substrate surface, it spreads out and is flattened. Under the appropriate conditions, the droplet may recoil prior to complete solidification due to surface tension forces, and spring back up while its lower surface remains attached to the substrate. As the droplet deforms it is cooled by the substrate and eventually solidifies. The relative time scales of the deformation, cooling and solidification processes are crucial in the determination of the ultimate droplet shape. This study focuses on the transport phenomena which occur during the impact process of a eutectic tin–lead solder (63% Sn–37% Pb) droplet.

Numerical efforts which focused on the fluid dynamics of the droplet impingement process initially adopted oversimplifying assumptions in order to facilitate solution. For example, Harlow and Shannon [2] neglected both viscous and surface tension effects in their modelling of a liquid droplet impacting on a flat plate. The "marker-and-cell" technique [3–5] based on a fixed grid was employed in the above work which pioneered the simulation efforts of the splashing process. Trapaga and Szekely [6] presented a numerical model which gave a detailed characterization of the droplet deformation process on a solid plate by treating the free surface deformation with a combination of the "marker-and-cell" and "volume-of-fluid" methods. A finite difference scheme in conjunction with a fixed computational grid was utilized

through the use the commercially available FLOW-3D software. A wide variety of data was produced on the effect of process parameters for high-speed, spray forming applications. Tsurutani *et al.* [7] also reported results from numerical simulations of droplet spreading on a flat surface. They based their work on the simplified marker-and-cell method (SMAC) and also employed a fixed grid.

Zhao *et al.* [8] recently completed modelling of the splat cooling of a liquid-metal droplet which accounted for the associated fluid dynamics phenomena, but in the absence of solidification. These authors used the Lagrangian formulation and extended the fluid dynamics model of Fukai *et al.* [9] to account for the heat transfer process in the droplet and the substrate. An experimental study was also completed by Zhao *et al.* [10] in which two-reference-beam pulse holography was utilized to visualize droplet deformation, and a novel photoelectric method was devised to record the radius of an impacting droplet as a function of time. In the numerical work, temperature fields were determined for liquid-metal and water droplets deposited on various substrate materials.

Gao and Sonin [11] presented a study of the deposition of molten microdrops for the following scenarios: single droplets, low and high frequency deposition of multiple droplets to produce columns, sweep deposition of continuous beads, and repeated sweep deposition to build layered objects. Experiments were carried out with candelilla and microcrystalline petroleum waxes using a modified ink-jet print head to produce microdrops with diameters on the order of 50 μm and impact velocities of approximately 3.0 m s^{-1}. A theoretical analysis was also performed in which order-of-magnitude approximations were made to define the time to remove the initial superheat, the time to remove the latent heat during freezing, and the time required to cool the deposit to the ambient temperature. Two effects which have been shown to be significant in other studies were neglected in the theoretical formulations: convection effects within the droplet [8] and thermal contact resistance at the splat–substrate interface [12–14].

The phenomena occurring during the impact of a single liquid-metal droplet on a cold substrate are neither conventional, nor easy to study. The fluid dynamics describing the droplet spreading is a free surface problem with large domain deformations in the presence of surface tension. The transient heat transfer process involves convection and solidification within a severely deforming domain, coupled with conduction in the substrate. Experimental investigation of the problem is quite challenging due to the very fast flow and thermal transients (on the microsecond scale) involved. Due to the difficulty of performing experiments which capture the transport processes during impact, a numerical model has been developed. The model is exercised in this study to demonstrate the impact of variations of the following: initial droplet temperature, impact velocity, thermal resistance at the droplet–substrate interface and initial substrate temperature. An experimental investigation of solidified droplets deposited under different conditions is also reported and compared to results obtained from the theoretical model.

2. THE MATHEMATICAL MODEL

2.1. *Fluids dynamics*

The mathematical model is formulated to simulate the impact of an initially spherical molten droplet on a substrate beginning at the instant of contact. It is based on the Navier–Stokes equations applied to the axisymmetric coordinate system shown in Fig. 2, in which r, z and θ are the radial, axial and azimuthal coordinates. Laminar flow of a constant property fluid is assumed, and the motion of the deforming free surface is simulated using the Lagrangian approach [9, 15]. The governing equations are formulated such that the radial and axial locations appear as dependent variables, while the independent variables are the fluid particle labels. The dimensionless forms of the governing equations are expressed as

$$\frac{\partial P}{\partial \tau} + \frac{1}{M^2}\left(\frac{1}{R}\frac{\partial}{\partial R}(RU) + \frac{\partial V}{\partial Z}\right) = 0 \tag{1}$$

$$\frac{\partial U}{\partial \tau} - \frac{1}{R}\frac{\partial}{\partial R}(R\bar{\sigma}_{RR}) - \frac{\partial \bar{\sigma}_{RZ}}{\partial Z} + \frac{1}{R}\bar{\sigma}_{\theta\theta} = 0 \tag{2}$$

$$\frac{\partial V}{\partial \tau} - \frac{1}{R}\frac{\partial}{\partial R}(R\bar{\sigma}_{ZR}) - \frac{\partial \bar{\sigma}_{ZZ}}{\partial Z} + \frac{1}{Fr} = 0 \tag{3}$$

$$U = \frac{\partial R}{\partial \tau} \tag{4}$$

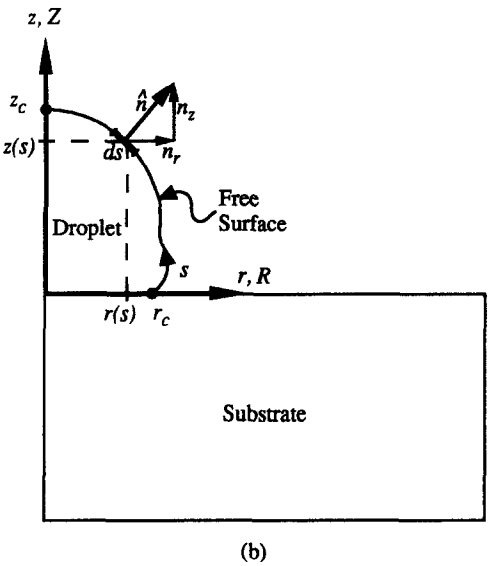

(b)

Fig. 2. Schematic of the problem of interest showing axisymmetric droplet coordinate definition with free surface detail.

$$V = \frac{\partial Z}{\partial \tau}. \tag{5}$$

With the Lagrangian formulation, convective terms do not appear in equations (2) and (3), eliminating the need for 'upwinding' in the numerical solution. The artificial compressibility method [16, 17] was employed, whereby an incompressible fluid is assumed to be 'slightly' compressible. To complete the model, dimensionless stress tensor terms are defined as

$$\bar{\sigma}_{RR} = -P + \frac{2}{Re}\frac{\partial U}{\partial R} \quad \bar{\sigma}_{\theta\theta} = -P + \frac{2}{Re}\frac{U}{R}$$

$$\bar{\sigma}_{RZ} = \bar{\sigma}_{ZR} = \frac{1}{Re}\left(\frac{\partial U}{\partial Z} + \frac{\partial V}{\partial R}\right) \quad \bar{\sigma}_{ZZ} = -P + \frac{2}{Re}\frac{\partial V}{\partial Z}. \tag{6}$$

The dimensionless initial and boundary conditions are (see Fig. 2)

$$\tau = 0 : R = R_0 \quad Z = Z_0 \quad U = 0 \quad V = -1$$

$$\text{and} \quad P = \frac{4}{We}$$

$$R = 0 : U = 0 \quad \frac{\partial V}{\partial R} = 0 \quad \text{and}$$

$$Z = 0 : \quad U = V = 0$$

along free surface:

$$\bar{\sigma}_{RR} n_R + \bar{\sigma}_{RZ} n_Z = -2\frac{\bar{H}}{We} n_R \quad \text{and}$$

$$\bar{\sigma}_{ZR} n_R + \bar{\sigma}_{ZZ} n_Z = -2\frac{\bar{H}}{We} n_Z \tag{7}$$

where n_r and n_z are the radial and axial components of the outward unit normal to the surface (see Fig. 2). The non-dimensionalization was performed according to the following definitions

$$R = \frac{r}{d_0} \quad Z = \frac{z}{d_0} \quad S = \frac{s}{d_0} \quad \bar{H} = \frac{H}{1/d_0}$$

$$\tau = \frac{t}{d_0/v_0} \quad U = \frac{u}{v_0} \quad V = \frac{v}{v_0} \quad P = \frac{p}{\rho_0 v_0^2} \quad \bar{\sigma}_{ij} = \frac{\sigma_{ij}}{\rho_0 v_0^2} \tag{8}$$

where the mean curvature, H, of the free surface is defined as

$$H = \frac{r^2(r'z'' - z'r'') + [(r')^2 + (z')^2]rz'}{2r^2[(r')^2 + (z')^2]^{3/2}}. \tag{9}$$

The prime in equation (9) indicates differentiation with respect to the arc length, s, which is defined in Fig. 2. The wetting force at the dynamic contact line between the liquid droplet and the substrate is neglected throughout this analysis. This assumption is valid during the initial stages of droplet impact where inertia forces are high with respect to the retarding forces of viscosity and surface tension. In the case of solder jetting, solidification is likely to occur very quickly at the contact area, eliminating the need for a wetting condition altogether. Based on the non-dimensionalization scheme outlined above, the Reynolds, Weber, Froude and Mach numbers are defined, respectively, as follows

$$Re = \frac{\rho v_0 d_0}{\mu} \quad We = \frac{\rho v_0^2 d_0}{\gamma}$$

$$Fr = \frac{v_0^2}{d_0 g} \quad \text{and} \quad M = \frac{v_0}{c}. \tag{10}$$

2.2. *Heat transfer*

The Lagrangian formulation is also used to construct the mathematical model for the conjugate heat transfer process in the droplet and the substrate. The relevant dimensionless energy conservation equations, as well as the initial and boundary conditions are defined as follows.

Energy equation in the droplet ($i = 1$) and in the substrate ($i = 2$):

$$C_i \frac{\partial \Theta_i}{\partial \tau} - \frac{1}{PrRe}\left[\frac{1}{R}\frac{\partial}{\partial R}\left(K_i R \frac{\partial \Theta_i}{\partial R}\right) + \frac{\partial}{\partial Z}\left(K_i \frac{\partial \Theta_i}{\partial Z}\right)\right] = 0. \tag{11}$$

Initial conditions in droplet and substrate regions:

$$\Theta_1(R, Z, 0) = 1, \quad \Theta_2(R, Z, 0) = 0. \tag{12}$$

Heat transfer from all exposed surfaces is neglected, and the substrate is assumed to be large, such that the following condition applies to the boundaries of both regions

$$\frac{\partial \Theta_i}{\partial R} n_r + \frac{\partial \Theta_i}{\partial Z} n_z = 0; \quad i = 1, 2. \tag{13}$$

The non-dimensionalization of temperature was carried out according to the following

$$\Theta_i = \frac{T_i - T_{2,0}}{T_{1,0} - T_{2,0}}; \quad i = 1, 2 \tag{14}$$

where subscripts 0, 1 and 2 indicate initial, droplet and substrate, respectively. The Prandtl number Pr, dimensionless heat capacity C_i, and thermal conductivity K_i, are defined as

$$Pr = \frac{\mu_0 c_{p,0}}{k_0} \quad C_i = \frac{\rho_i c_{p,i}}{\rho_o c_{p,0}} \quad \text{and} \quad K_i = \frac{k_i}{k_0}. \tag{15}$$

Contact resistance between the droplet and substrate regions is modeled by a thin layer of arbitrary thickness, l_0, which attaches the two regions. This layer is assigned zero heat capacity and experiences only axial conduction. The effective layer axial thermal conductivity, $k_{zz,c}$, is related to the contact heat transfer coefficient by

$$k_{zz,c} = h_c l_c. \tag{16}$$

The resulting dimensionless energy equation for the layer is

$$C_c\frac{\partial\Theta}{\partial\tau}-\frac{1}{PrRe}\left[\frac{1}{R}\frac{\partial}{\partial R}\left(K_{rr,c}R\frac{\partial\Theta}{\partial R}\right)+\frac{\partial}{\partial Z}\left(K_{zz,c}\frac{\partial\Theta}{\partial Z}\right)\right]=0 \quad (17)$$

where $C_c = 0$ and $K_{rr,c} = 0$. Non-dimensionalization of equation (16) yields

$$K_{zz,c}=\frac{h_0 d_0}{k_0}\frac{l_c}{d_0}=\bar{h}_c L_c \quad (18)$$

where $\bar{h}_c$ and L_c are the dimensionless layer heat transfer coefficient and thickness, respectively.

Three assumptions are made with regard to the solidification of the droplet. First, since a eutectic alloy is under study, a sharp boundary separating distinct liquid and solid regions is included in the model. It is further assumed that phase change occurs at the equilibrium freezing temperature, T_m. Lastly, the droplet solid and liquid phase densities are assumed to be identical since the 63% Sn–37% Pb material experiences only a 2.4% contraction upon freezing.

The exact specific heat method proposed by Bushko and Grosse [18] was utilized to model solidification. In this approach the specific heat of the droplet material is defined as

$$c_{p,l}(T_l)=\{c_{ps,l}(T_l<T_m),c_{pl,l}(T_l>T_m)\}+L\delta(T_l-T_m) \quad (19)$$

where L is the latent heat of fusion, δ is the Dirac delta function and the subscripts s and l refer to solid and liquid, respectively. The approach proposed by Bushko and Grosse [18] leads to exact integration of the capacitance terms in the finite element formulation with linear triangle elements. The advantage of this approach is that it very accurately conserves energy as the droplet solidifies. The dimensionless droplet heat capacity is written as

$$C_l(\Theta_l)=\{C_{l,s}(\Theta_l<\Theta_m),C_{l,l}(\Theta_l>\Theta_m)\}+\frac{1}{Ste}(1-\mathrm{SHP})\delta(\Theta_l-\Theta_m) \quad (20)$$

where the Stefan number Ste and the superheat parameter SHP are defined as

$$Ste=\frac{c_{pl,l}(T_m-T_{2,0})}{L} \quad \text{and} \quad \mathrm{SHP}=\frac{(T_{1,0}-T_m)}{(T_{1,0}-T_{2,0})}. \quad (21)$$

3. NUMERICAL SOLUTION PROCEDURE

The computational domain was discretized with a mesh of triangular elements (six-node elements for the flow solution and three-node thermal elements for the heat transfer solution), and the numerical model was solved using a Galerkin finite element method. Quadratic and linear shape functions were used for velocity and pressure, respectively. Each six-node element was subdivided into four three-node elements by connecting mid-side nodes to solve the energy equation in the droplet. An implicit method was utilized for the numerical integration of the fluid dynamics equations in time, while a Crank–Nicholson scheme was used for the energy equation. The fluid particle locations and the conservation equations were coupled using a method proposed by Bach and Hassager [15]. The following summarizes a single time step in the computation.

(1) Given an initial configuration of fluid particles and flow variables, calculate the new nodal locations by numerical interation of equations (4) and (5). The velocities at time τ are used as initial 'guesses' for velocities at time $\tau+\Delta\tau$.

(2) Based on current nodal locations, calculate velocity and pressure fields by solving the discrete forms of equations (1)–(3).

(3) Update the nodal locations by numerical interation of equations (4) and (5) after inserting the velocities at time step τ and $\tau+\Delta\tau$.

(4) Iterate steps (2) and (3) until convergence is reached for the time step. Convergence was assumed when the maximum difference for each fluid particle flow variable was less than 0.1% from one iteration to the next.

(5) Given the temperature field at time τ, solve the equation (11) to obtain the overall temperature field at time $\tau+\Delta\tau$ in all regions simultaneously.

(6) If solidification modeling is included, the velocities of droplet nodes for which $\Theta_l < \Theta_m$ are set to zero for the next time step.

As the impact simulation proceeds in time, the elements become increasingly distorted. To reduce solution inaccuracies due to this distortion, a new mesh was created when any one of the following conditions was met for an element: (a) a vertex angle α_j at corner node j fell outside the range $15^\circ < \alpha_j < 130^\circ$; (b) a mid-side node was placed within one third of the distance to a vertex node; (c) the Jacobian distortion ratio $(\Sigma_{l=1}^{7} w_l J_l)/J_l$ exceeded 1.8 for a Gauss point, where J_l is the element Jacobian and w_l is the Gauss weight. The mesh generation technique used is an advancing front method adapted from Peraire *et al.* [19]. Once a new mesh was created, the solution variables were mapped to the new nodes via interpolation on the old mesh. A detailed study was performed by Waldvogel [20] to determine the temporal and spatial discretization necessary to obtain time step and grid insensitive solutions. The initial mesh contained 604 nodes and 275 six-node elements in the droplet, and 1154 nodes and 2095 three-node elements in the substrate. A dimensionless time step of 5×10^{-4} was employed, and an example simulation required 54

CPU h to complete 7950 time steps on a Hewlett Packard 9000 Series 735 workstation.

4. EXPERIMENTAL PROCEDURES

A simplified schematic of the experimental solder jetting apparatus which was used to generate solder deposits was shown earlier in Fig. 1. The cylindrical assembly shown in this figure is made up of two components: the upper heated reservoir and the droplet generator device mounted below. Overall, the size of the assembly is small, approximately 50 mm in diameter and about 150 mm in height. High-purity 63%Sn–37%Pb solder is melted in the reservoir section and maintained at 210°C during experimentation. Nitrogen gas is used to pressurize the system to aid in the formation of droplets and to hinder the formation of oxides within the reservoir. The lower section is comprised of the droplet generator itself, which is surrounded by a heated shroud. Individual droplets are generated as a voltage pulse excites the transducer mounted within. The assembly shown in Fig. 1 is mounted to a Universal Instruments high-accuracy XY placement system. With the aid of a version system, the solder jet print head assembly is moved into position above the stationary substrate with a placement accuracy of ± 0.013 mm. The motion of the print head and the operation of the droplet generator are controlled by personal computer. To determine the velocity at impact, a steady stream of droplets is generated at a known frequency (250 drops s^{-1} in this experiment). A stroboscope is used to 'freeze' the droplet motion, which is recorded using a CCD (Charge Coupled Device) camera, thereby determining the velocity.

5. RESULTS AND DISCUSSION

5.1. *Simulation results for an impacting droplet with solidification*

First, the time-dependent behavior of a baseline case comprised of typical solder jetting conditions will be examined in detail. The conditions for the baseline case are as follows: a 50 μm, 63%Sn–37%Pb solder droplet with initial temperature $T_{1,0} = 200°C$ and impact velocity $v_0 = 1.5$ m s^{-1} impinges on an 8.9 μm thick layer of copper on a thick layer of FR-4 circuit board material. The entire substrate has initial temperature $T_{2,0} = 25°C$, and the interface between the droplet and the substrate is characterized by the interfacial heat transfer coeeficient $h_c = 2.5 \times 10^4$ W m^{-2} K^{-1}. The following thermophysical properties are used for liquid phase of the solder: surface tension coefficient $\gamma_l = 0.345$ N m^{-1}, density $\rho_l = 8218$ kg m^{-3}, viscosity $\mu_l = 0.00262$ kg m^{-1} s^{-1}, specific heat $c_{p,l} = 238$ J kg^{-1} K^{-1}, and thermal conductivity $k_l = 25$ W m^{-1} K^{-1}. The solid phase thermophysical properties are as follows: phase transition temperature $T_m = 183°C$, thermal conductivity $k_s = 48$ W m^{-1} K^{-1}, density $\rho_s = 8218$ kg m^{-3}, specific heat $c_{p,s} = 176$ J kg^{-1} K^{-1} and latent heat of fusion $L = 42\,000$ J kg^{-1}. With regard to the substrate materials, the density, thermal conductivity and specific heat used are 8933 kg m^{-3}, 401 W m^{-1} K^{-1} and 385 J kg^{-1} K^{-1} for copper and 1924 kg m^{-3}, 0.26 W m^{-1} K^{-1} and 1570 J kg^{-1} K^{-1} for the FR-4 material.

Figure 3 shows a sequence of frames from a simulation of the baseline case which encompasses the initial impact through complete solidification. The dimensionless parameters which define this case are: $Re = 235$, $We = 2.68$, $Fr = 4592$, $Ste = 0.895$, $Pr = 0.025$, SHP $= 0.0971$, $\Theta_m = 0.903$ and $\bar{h}_c = 0.05$. In each frame the droplet boundary, velocity distribution and freeze front (if present) are plotted with respect to the dimensionless coordinates R and Z. The temperature distribution is not displayed because the droplet and substrate regions were each approximately isothermal during the steps shown; that is, the substrate temperature remained almost entirely uniform at $\Theta_2 = 0.0$ and the droplet temperature varied only with time (approximately) between the values $\Theta_1 = 1.0$ and $\Theta_1 = 0.903$. This behavior is due to the contact resistance which impedes heat flow between the two regions. It is apparent in Fig. 3 that the droplet experiences significant deformation prior to the onset of solidification at $t = 25.8$ μs. The droplet flattens, and begins to recoil toward the Z-axis before phase change begins at the droplet–substrate boundary. As the fluid continues to recoil and subsequently oscillate, the freeze front maintains a nearly planar shape while it moves upward. As the front propagates, it freezes the deforming droplet in various stages of oscillation.

While the freeze front is predominantly planar during this simulation, there are occasions when the fluid motion distorts this shape. For example, at $t = 73.3$ μs (see Fig. 3), as the fluid bulges outward over the solidified portion of the deposit, the freeze front propagation slows drastically near the free surface. However, in the vicinity of the Z-axis, the front continues to move upward at a steady rate. As a result, the front is curved downward near the outer boundary of the droplet from $t = 73.3$ μs to $t = 80.8$ μs. The front then flattens as the fluid flows radially inward, thereby eliminating the bulging region. At $t = 95.8$ μs (see Fig. 3), the droplet is in a third cycle in which the flow is directed radially outward. During this cycle, the inertial forces of the flow have been sufficiently dissipated by the effects of viscosity and surface tension, such that the droplet does not deform as far in the radial direction. Consequently, the front remains nearly flat until $t = 111$ μs, when it begins to curve upward as the droplet oscillations dampen, and complete solidification is reached at $t = 124$ μs.

In the following subsections, simulation results will be presented which demonstrate the response of a solidifying droplet to variations of: impact velocity, initial droplet temperature, contact heat transfer coefficient and substrate temperature. A more detailed study was presented by Waldvogel [20], in which the

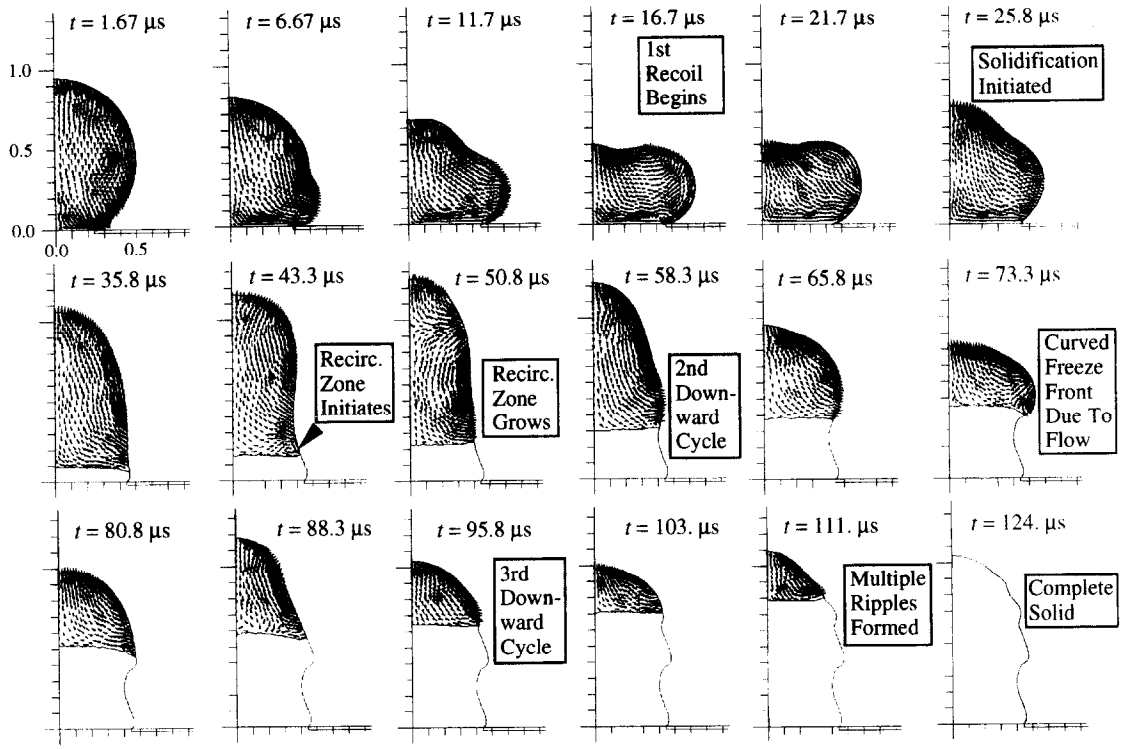

Fig. 3. Droplet shape, velocity distribution and freeze front location as a function of time for a 63% Sn–37% Pb droplet on FR-4–copper with $d_0 = 50\ \mu m$, $v_0 = 1.5\ m\ s^{-1}$, $h_c = 2.5 \times 10^4\ W\ m^{-2}\ K^{-1}$, $T_{1,0} = 200.0°C$ and $T_{2,0} = 25.0°C$.

effects of additional process variations are considered. All of the parameters varied in this study, with the exception of the contact heat transfer coefficient, are clearly defined; that is, they can be obtained experimentally and their inclusion in a numerical model is straightforward. No correlations published to date have been identified which facilitate the prediction of h_c for the parametric domain of solder jetting. In this study, the convention introduced by Liu *et al.* [21] has been utilized, whereby two interfacial heat transfer coefficients are specified: $h_{c,s}$ and $h_{c,l}$. The subscript l indicates liquid droplet material is in contact with the substrate, while the subscript s indicates solid droplet material is in contact. Numerical values for $h_{c,s}$ and $h_{c,l}$ were determined experimentally by Liu *et al.* [21] to be in the range 10^3–$10^4\ W\ m^{-2}\ K^{-1}$, with $h_{c,l} > h_{c,s}$, for splat cooling of relatively large (5 mm) nickel droplets on various substrates. Unfortunately, these experiments were performed under conditions outside of the parametric domain of solder jetting, and no empirical correlation was developed for the prediction of h_c. Recently, Wang and Matthys [22] presented the results of experimentation similar to that performed by Liu *et al.* [21], but with improved equipment. Heat transfer coefficients were quantified for three different phases of droplet impact: during liquid–solid contact, during solidification and during solid–solid contact after solidification. This recent research activity indicates that the exact value of h_c is not clearly understood, especially for the conditions consistent with solder jetting. Consequently, reasonable values for h_c were specified based on the work of Liu *et al.* [21] to obtain the numerical results which follow. The sensitivity of the solution to variations in this parameter is also presented.

5.2. *Effect of impact velocity and droplet temperature*

A matrix of 21 simulations was performed to study the effects of impact velocity and initial droplet temperature with all other dimensional conditions held constant at the baseline values. The final solidified shapes for 15 of these runs are shown in Fig. 4, which is arranged with increasing droplet temperature at impact from left to right, and decreasing impact velocity from top to bottom. The initial temperature was varied between 185°C and 215°C at 5°C intervals, while three impact velocity conditions were simulated: $v_0 = 1.5$, 1.7 and 2.0 m s^{-1}. These velocities correspond to the following dimensionless parameters, which are listed in the same order: $Re = 235$, 267, 314 and $We = 2.68$, 3.44, 4.76. Similarly, the initial temperature cases shown in Fig. 6 (185, 195, 200, 205 and 215°C) correspond to the following dimensionless groups: $Ste = 0.895$, $\Theta_m = 0.988$, 0.929, 0.903, 0.878, 0.832 and SHP = 0.0125, 0.0706, 0.0971, 0.122, 0.168. In each case, the time to reach complete solidification measured from initial impact is also provided in dimensional and dimensionless terms: t_{cs} and τ_{cs}, respectively. Results based on variation of both v_0 and $T_{1,0}$ are provided in Fig. 4 because there appears to be

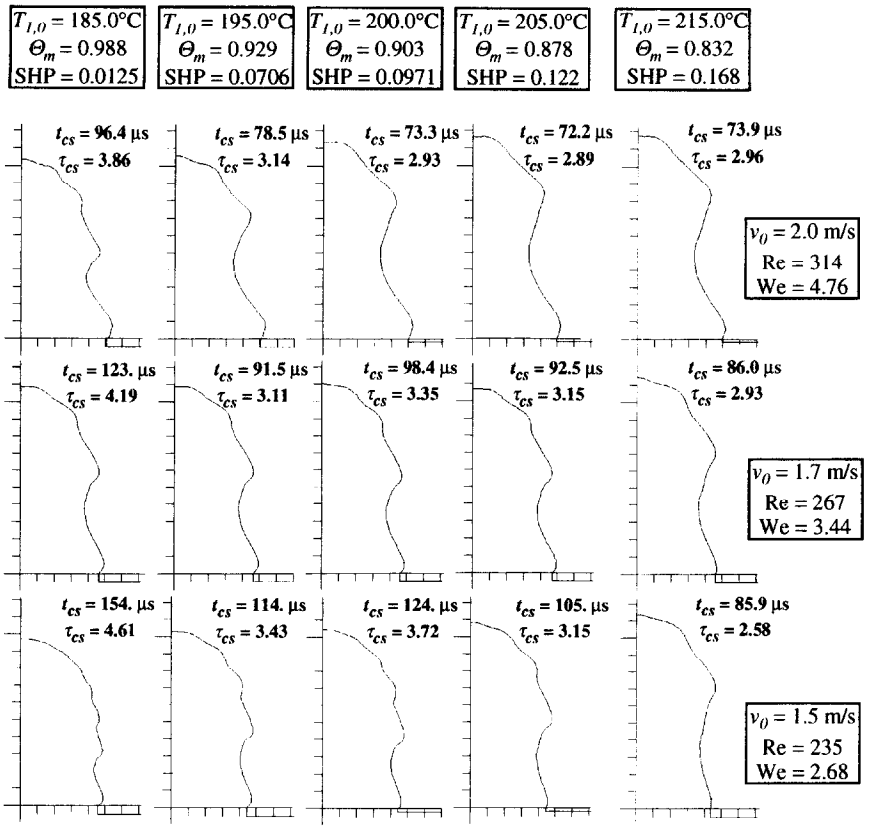

Fig. 4. Final solidified shapes for 63% Sn–37% Pb droplet on FR4–copper with $d_0 = 50$ μm, $h_{c,l} = 2.5 \times 10^4$ W m^{-2} K^{-1}, $h_{c,s} = 2.5 \times 10^4$ W m^{-2} K^{-1} and $T_{2,0} = 25.0$°C.

coupling of the effects for these two variables. For example, t_{cs} decreases monotonically with increasing droplet temperature overall, but t_{cs} reaches a local maximum at $T_{1,0} = 200$°C for both $v_0 = 1.5$ and 1.7 m s^{-1}. It is clear that variations of either v_0 or $T_{1,0}$ can affect the wavy surface which results. A reduction of the initial droplet temperature leads to more surface ripples and a decrease in the spacing between the ripples for all velocity conditions shown in Fig. 4. Similarly, for all temperature cases shown, a reduction of impact velocity also results in an increase in the number of ripples and a decrease in ripple spacing.

In order to investigate the effects of $T_{1,0}$ and v_0 on the freezing behavior more closely, t_{cs} is divided into two components: t_{is} is the time measured from initial impact to the onset of solidification, and t_s is the time measured from the onset to the completion of solidification. Dimensionless times, τ_{is} and τ_s, are similarly defined. In Fig. 5(a), t_{is} is plotted as a function of the initial droplet temperature for the three velocity cases. Clearly, the time to initiate freezing rises uniformly with increasing $T_{1,0}$ for each velocity condition because the amount of superheat which must be overcome also increases uniformly. Also, the initiation time t_{is} decreases monotonically with increasing impact velocity (fixed $T_{1,0}$) due to the corresponding increase in the contact area between the droplet and the substrate, as well as the additional cooling effects of enhanced fluid convection. The solidification time t_s is shown as function of initial droplet temperature in Fig. 5(b) for $v_0 = 1.5$, 1.7 and 2.0 m s^{-1}. In this figure, a nonmonotonic dependence of t_s on $T_{1,0}$ is apparent, although t_s generally decreases with increasing $T_{1,0}$, except for local maxima which occur at $T_{1,0} = 200$°C for $v_0 = 1.5$ and 1.7 m s^{-1}. The magnitudes of these local maxima reduce with increasing velocity, and the peak disappears at $v_0 = 2.0$ m s^{-1}. To resolve this behavior, the droplet shape and velocity distribution are shown in Fig. 6 at the onset of freezing. The droplet is in a clearly different state of deformation for each case, although the initial droplet temperature appears to be the more dominant parameter. With regard to the impact velocity, the most apparent differences occur at $T_{1,0} = 195$°C and 200°C when the $v_0 = 1.5$ and 1.7 m s^{-1} cases are compared to the $v_0 = 2.0$ m s^{-1} case. This range of v_0 and $T_{1,0}$ corresponds to the parametric domain in which t_s experiences a temporary increase with respect to $T_{1,0}$ in Fig. 5(b), which indicates a relationship between the droplet dynamics and the freezing time.

In order to capture some quantitative measure of the droplet deformation, the dimensionless height of the second droplet surface ripple $Z_{r,2}$ (which is defined in Fig. 7) is plotted as a function of initial droplet

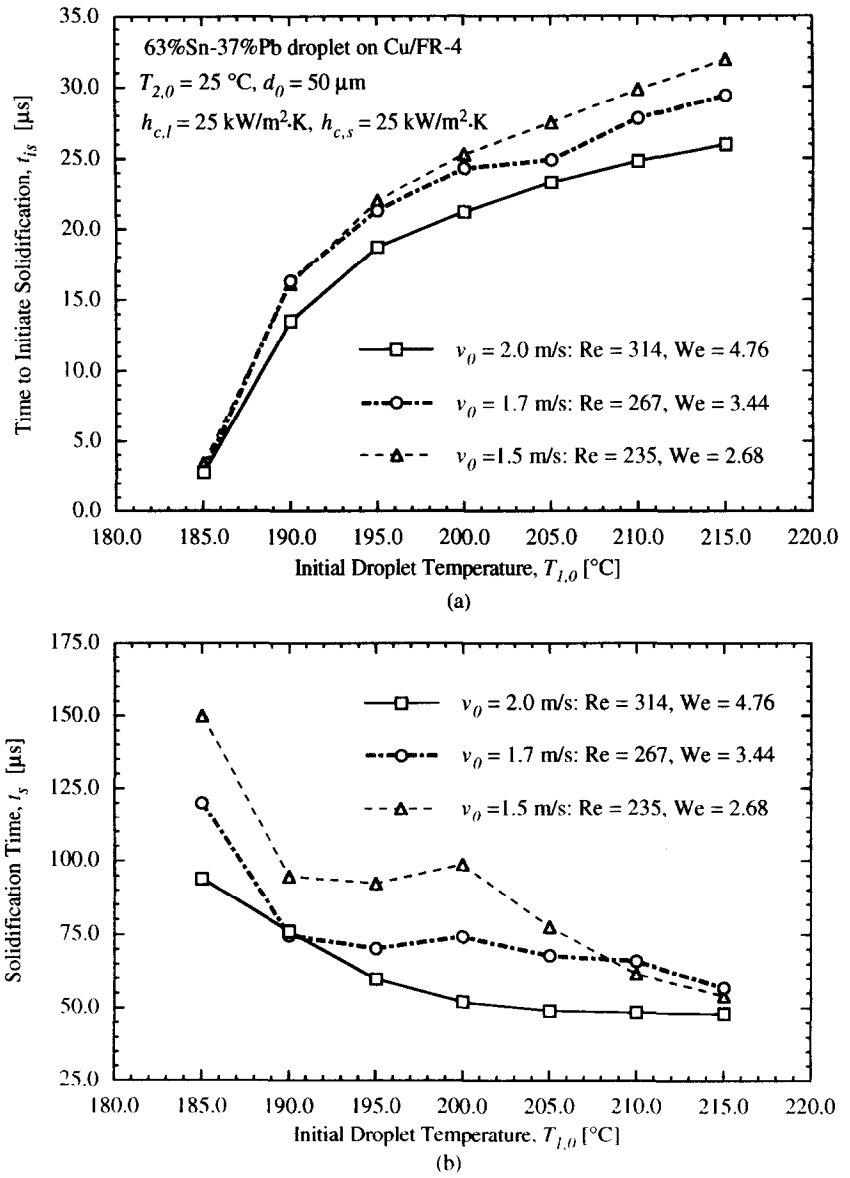

Fig. 5. Solidification times as functions of initial droplet temperature: (a) time to initiate solidification; (b) time to complete solidification.

temperature for v_0 = 1.5 and 2.0 m s^{-1} in Fig 7. The solidification time t_s is also plotted in these figures with its associated scale on the right vertical axis to highlight the relationship between freezing time and droplet deformation. A clear trend is evident in each of these figures which provides an explanation for the nonmonotonic behavior exhibited in Fig. 5(b): the solidification time increases when the height of the second ripple decreases and, conversely, the solidification time decreases when the height increases. Consequently, the time required to freeze the droplet depends on the states of deformation 'captured' by the solidification process. Since the droplet deformation demonstrates a complex, nonmonotonic dependence on process parameters, it is not surprising that the freezing time responds in a similar fashion.

5.3. *Effect of interfacial contact resistance*

The effect of the interfacial contact resistance on the solidifying droplet was investigated in four simulations in which the liquid and solid contact heat transfer coefficients, $h_{c,l}$ and $h_{c,s}$, were varied while the other run parameters were maintained at the baseline conditions. In three of the simulations, the liquid contact heat transfer coefficient was fixed at $h_{c,l}$ = 25 kW m^{-2} K^{-1}, while the solid contact value was varied as $h_{c,s}$ = 5, 10 and 25 kW m^{-2} K^{-1}. For the fourth simulation, the values $h_{c,l} = h_{c,s}$ = 10 kW m^{-2} K^{-1} were chosen. Results for the four cases are summarized in Fig. 8, which shows the droplet shape, velocity distribution and freeze front location for three different time steps during each simulation: at the onset of freezing, an intermediate step τ = 2.0 and the final

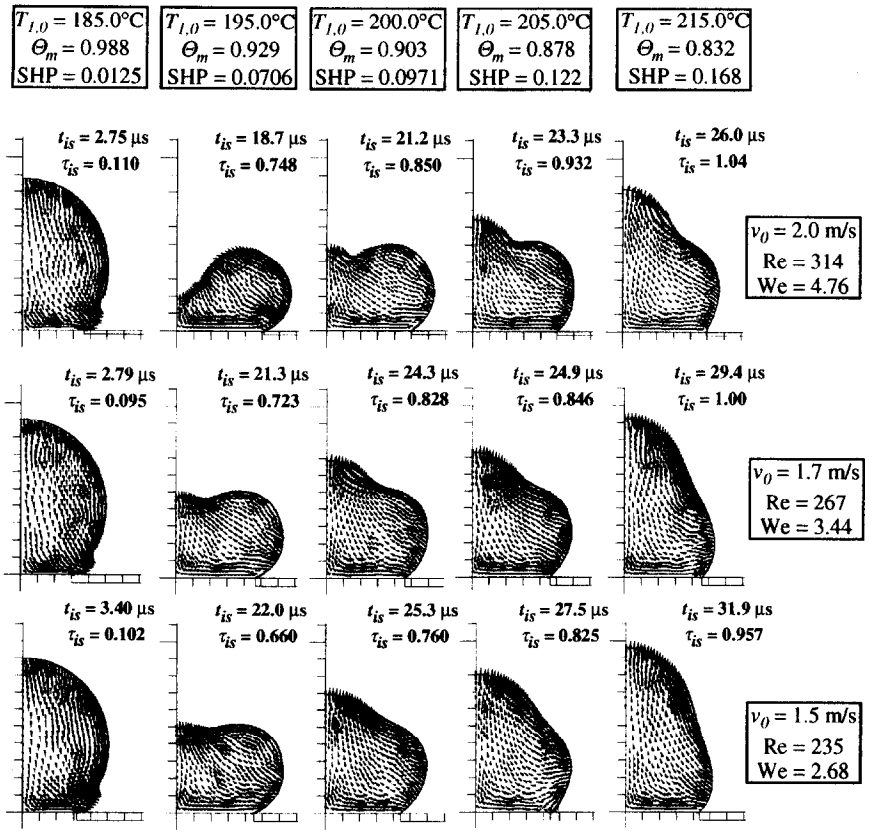

Fig. 6. 63% Sn–37% Pb droplet configuration on FR-4–copper at onset of solidification with $d_0 = 50$ μm, $h_{c,l} = 2.5 \times 10^4$ W m^{-2} K^{-1}, $h_{c,s} = 2.5 \times 10^4$ W m^{-2} K^{-1} and $T_{2,0} = 25.0$°C.

solidified state. In this figure, the heat transfer coefficient variations are arranged horizontally, while the three time steps are arranged vertically.

The impact of decreasing $h_{c,l}$ on the initiation of freezing is as would be expected: The onset of phase change is delayed from $t_{is} = 25.3$ μs for $h_{c,l} = 25$ kW m^{-2} K^{-1} to $t_{is} = 35.4$ μs for $h_{c,l} = 10$ kW m^{-2} K^{-1} (see top row of images in Fig. 8). As a result of this delay, the droplet recoils further for $h_{c,l} = 10$ kW m^{-2} K^{-1}, such that the contact angle at the droplet–substrate interface is approximately 90°, compared to about 135° for the $h_{c,l} = 25$ kW m^{-2} K^{-1} cases. The propagation of the freezing front is impeded more as $h_{c,s}$ is reduced in the order 25, 10 and 5 kW m^{-2} K^{-1}. The impediment of the freezing process is quantified by the reduction of the solid fraction α_s, which is provided in Fig. 8 for $\tau = 2.0$. A closer examination of the $h_{c,l} = 25$ kW m^{-2} K^{-1} cases at $\tau = 2.0$ also reveals that the different solidification rates lead to the different droplet dynamics. For example, the Z-axis contact point is lower in the $h_{c,s} = 25$ kW m^{-2} K^{-1} case, and the top surface of the droplet assumes more of a rounded shape.

Examination of the final solidified shapes in Fig. 8 for the three cases for which $h_{c,l} = 25$ kW m^{-2} K^{-1} indicates that the surface ripples occur closer to the substrate and with closer spacing as the solid contact heat transfer coefficient is reduced. As would be expected, the solidification time also increases as $h_{c,s}$ is reduced due to the increase in the thermal resistance. Also the solidification time t_s decreases as the height of the second ripple increases. Even though the final shapes of the $h_{c,l} = h_{c,s} = 10$ kW m^{-2} K^{-1} and $h_{c,l} = h_{c,s} = 25$ kW m^{-2} K^{-1} cases differ, the solidification times t_s are nearly identical. It is also surprising that the solidification time for the $h_{c,l} = h_{c,s} = 10$ kW m^{-2} K^{-1} case is less than that of the case in which $h_{c,l} = 25$ kW m^{-2} K^{-1} and $h_{c,s} = 10$ kW m^{-2} K^{-1}. For the latter condition, one may expect the enhanced heat transfer during the initial phases of the simulation (when liquid material is in contact with the substrate) would lead to a faster overall solidification rate. Actually, the opposite occurs. As previously mentioned, the higher value of $h_{c,l}$ results in the earlier initiation of phase change; however, the droplet motion which follows for the $h_{c,l} = h_{c,s} = 10$ kW m^{-2} K^{-1} case leads to more rapid freezing. The final solidified shapes for these two cases contain a feature observed in other simulations which supports this surprising result. When $h_{c,l} = h_{c,s} = 10$ kW m^{-2}

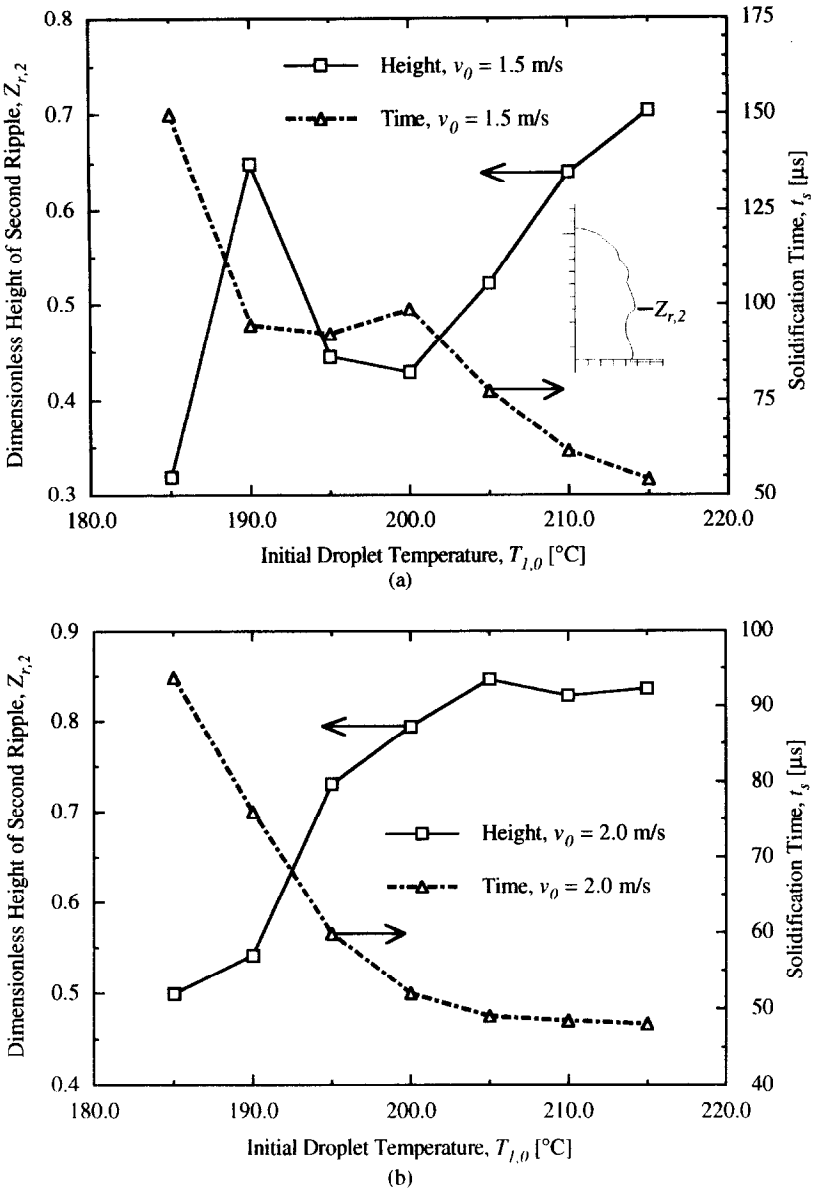

Fig. 7. Dimensionless height of second ripple and solidification time as functions of initial droplet temperature for: (a) $v_0 = 1.5$ m s^{-1}; and (b) $v_0 = 2.0$ m s^{-1}.

K^{-1}, the height of the second ripple is greater, which has been demonstrated to be indicative of a shorter solidification time.

5.4. *Effect of initial substrate temperature*

Five simulations were performed in which the temperature of an FR-4–copper substrate was increased from 25°C to 125°C at 25°C intervals, while baseline values were maintained for the remaining simulation conditions. Results for two time steps for each simulation are provided in Fig. 9, in which the images are arranged with increasing initial substrate temperature from left to right. The top row of images in this figure corresponds to the onset of phase change. The dimensional and dimensionless times corresponding to the initiation event are also provided. The bottom row of images shows the final droplet shape in each simulation.

In Fig. 9 it is clear that the increase in substrate temperature delays the onset of freezing in a monotonically increasing fashion. As a result, the droplet recoils further with each increase in $T_{2,0}$. With the oscillatory motion of the liquid phase of the droplet shown in Fig. 3 in mind, it is quite conceivable that for the appropriate combination of conditions (particularly an elevated substrate temperature and/or significant interfacial thermal contact resistance), the initiation of freezing could be delayed until the droplet experiences a second downward cycle. By examining the final solidified shapes in Fig. 9, the impact of the delay of freezing due to the increase of the substrate temperature is clear. The droplet–substrate contact

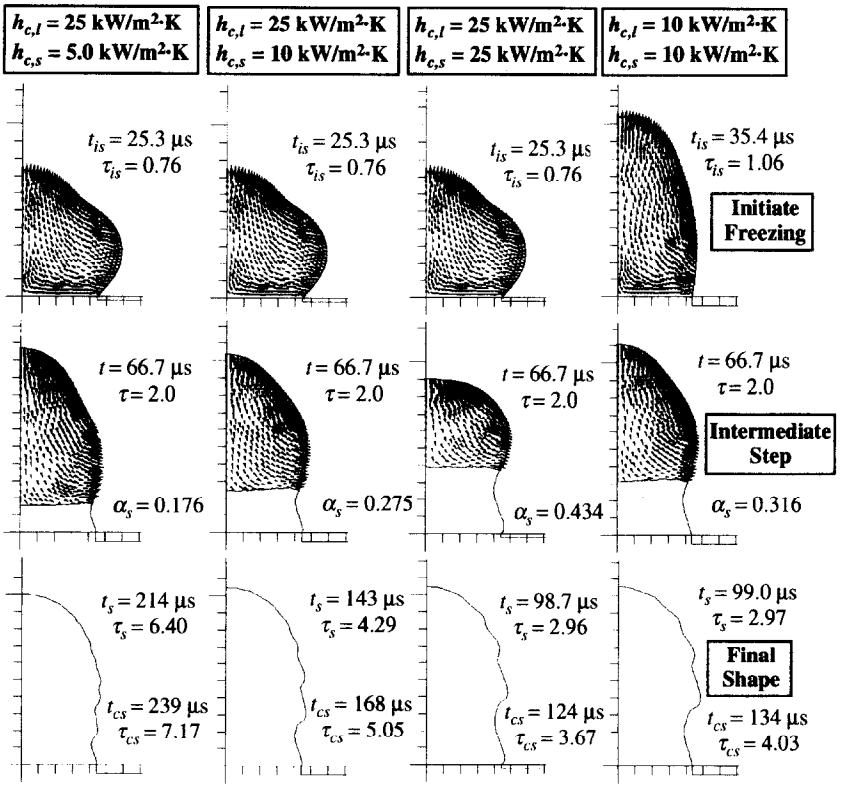

Fig. 8. Droplet configurations at various stages of freezing for a 50 μm, 63% Sn–37% Pb droplet on FR-4–copper (8.9 μm) for different contact heat transfer coefficients with v_0 = 1.5 m s^{-1}, $T_{1,0}$ = 200.0°C and $T_{2,0}$ = 25.0°C.

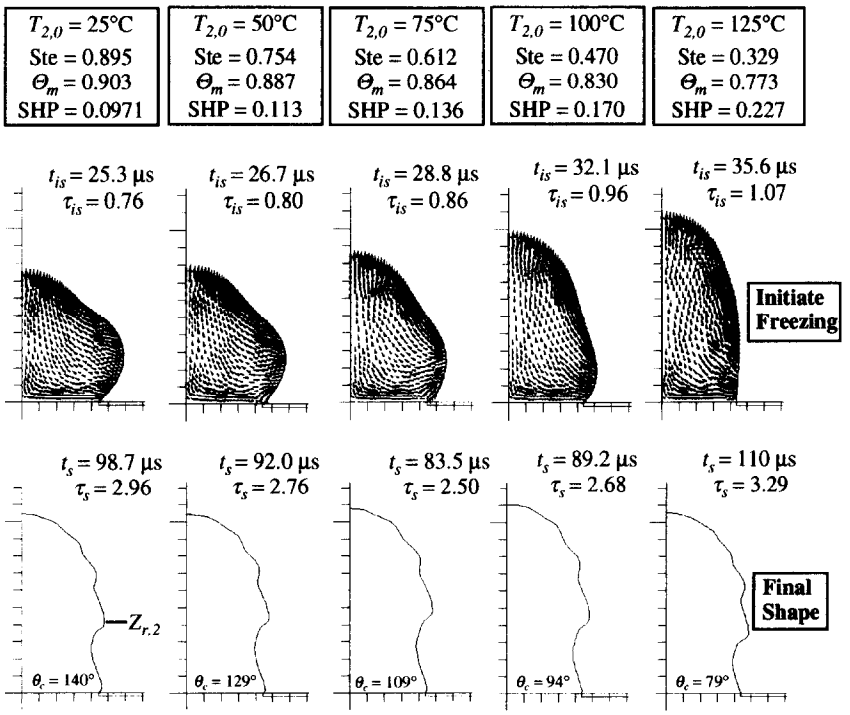

Fig. 9. Droplet configuration at onset and completion of solidification as a function of initial substrate temperature for a 50 μm 63% Sn–37% Pb droplet deposited on an FR-4–Cu substrate with v_0 = 1.5 m s^{-1}, $h_{c,l}$ = 2.5 × 10^4 W m^{-2} K^{-1}, $h_{c,s}$ = 2.5 × 10^4 W m^{-2} K^{-1}, $T_{1,0}$ = 200.0°C.

angle is shown in this figure as further evidence that droplet is in an advancing state of recoil with each increase in $T_{2,0}$. A familiar relationship between the height of the second surface ripple and the solidification time is also apparent. As $T_{2,0}$ is increased from 25°C to 75°C, $Z_{r,2}$ increases steadily, while t_s decreases steadily. However, between 75°C and 125°C, $Z_{r,2}$ decreases with a corresponding increase in t_s.

5.5. *Experimental study of substrate temperature effects*

A qualitative experimental investigation of the effect of the substrate temperature on the final solidified shape of the solder bumps produced was performed. More detailed quantitatitive analyses of the experimental findings are presented by Waldvogel [20]. The substrate used in this experiment was a 678 μm thick silicon wafer upon which the following metallization layers were applied in order: 0.08 μm chromium, 0.3 μm copper, 2.0 μm nickel and 0.1 μm gold. The droplets were deposited on the gold layer in 10×10 arrays with a pitch of 250 or 300 μm. During the deposition process, the solder reservoir temperature was maintained at 210°C and the jetting velocity was set at 1.5 m s^{-1}. The distance between the bottom of the droplet generator and the substrate was 0.5 mm, while the substrate temperature was varied between 35°C and 115°C at 10°C intervals. After deposition, a Hitachi model 570 scanning electron microscope was used to examine both arrays and individual solder deposits. Black and white photomicrographs were produced with a Polaroid 4×5 in film holder mounted to the microscope.

In Fig. 10, micrographs are provided of a representative droplet for each substrate temperature case between 35°C and 115°C. The axisymmetric approximation used in the numerical model is clearly appropriate as these isometric views of experimental deposits show no significant angular variation of the deposit surface. Droplets deposited at lower substrate temperatures clearly exhibit the wavy surface which was evident in the numerical simulation shown in Fig. 3. The simulation showed that this surface feature was created as the droplet was frozen in various stages of oscillation. Also, the size of the surface ripples, as well as the spacing between them, decrease with increasing distance from the substrate in both the experiment and the simulation.

Throughout the range of substrate temperature shown, the locations of the surface ripples move down toward the substrate as $T_{2,0}$ increases. The size of and the spacing between the ripples also decreases as $T_{2,0}$ increases. In the substrate temperature range $35°C \leqslant T_{2,0} \leqslant 85°C$, the shapes of the deposits are similar, and four distinct surface ripples are visible. However, at $T_{2,0} = 85°C$ [Fig. 10(f)] there appears to be a transition in droplet behavior as the general shape changes, and the substrate contact area decreases. At $T_{2,0} = 95°C$ [Fig. 10(g)] the general shape is again wider at the contact area, but only three surface ripples are apparent. The droplets corresponding to the $T_{2,0} = 105°C$ and 115°C substrate cases are also wider at the base; however, the surface ripples diminish, and at $T_{2,0} = 115°C$ the ripples are no longer distinct. Another interesting feature is the occurrence of a 'dimple' at the top of the droplet $T_{2,0} = 105°C$ and 115°C. This feature was present in each deposit in both 10×10 arrays. Based on the oscillatory droplet dynamics revealed by the numerical modelling, it is felt that the 'dimple' is created as the front (which has propagated further in the center than at the droplet periphery) reached the top of the droplet first, and the remaining fluid recoiled upward prior to freezing.

The apparent transition in droplet behavior which occurs at $T_{2,0} = 85°C$ [see Fig. 10(f)] requires further examination. As the substrate temperature is increased up to 85°C, the surface ripples clearly move down toward the substrate, and the droplet-substrate contact angle (measured within the droplet) decreases monotonically. At $T_{2,0} = 96°C$ [Fig 10(g)], the contact angle increases to a value greater than 90°, and only three surface ripples are visible. These trends were observed in the substrate temperature analysis performed with the numerical model in the previous subsection. For example, in Fig. 9, as the substrate temperature is increased in the order 75°C, 100°C, 125°C, the surface ripples move downward, and the contact angle decreases in the order $\theta_c = 109°, 94°, 70°$. The impact of increasing the substrate temperature is to delay the solidification with respect to the recoil of the droplet. This delay can reach a point such that the droplet fully recoils and begins a second downward cycle. A droplet which is frozen at the substrate during this second downward cycle would be wider at the base and would possess a contact angle greater then 90°. Based on the droplet dynamics observed in the numerical model and the experimentally observed changes in the droplet shape, it is concluded that the behavior described above is responsible for the apparent transition which occurs at $T_{2,0} = 85°C$.

6. CONCLUSIONS

A predominantly theoretical study of the transport processes associated with the impact and solidification of molten solder droplets on a multi-layer substrate was presented. This problem is of central importance to the novel micromanufacturing process called solder jetting, in which picoliter-size solder droplets are dispensed for the attachment of microelectronic components. The theoretical model which was developed using a Lagrangian formulation accounted for a host of thermal-fluid phenomena, and was solved utilizing the finite element method with a deforming grid. An experimental investigation was also presented in which deposits produced by a prototype solder jetting apparatus were analysed using scanning electron microscopy.

The results of many simulation cases were presented

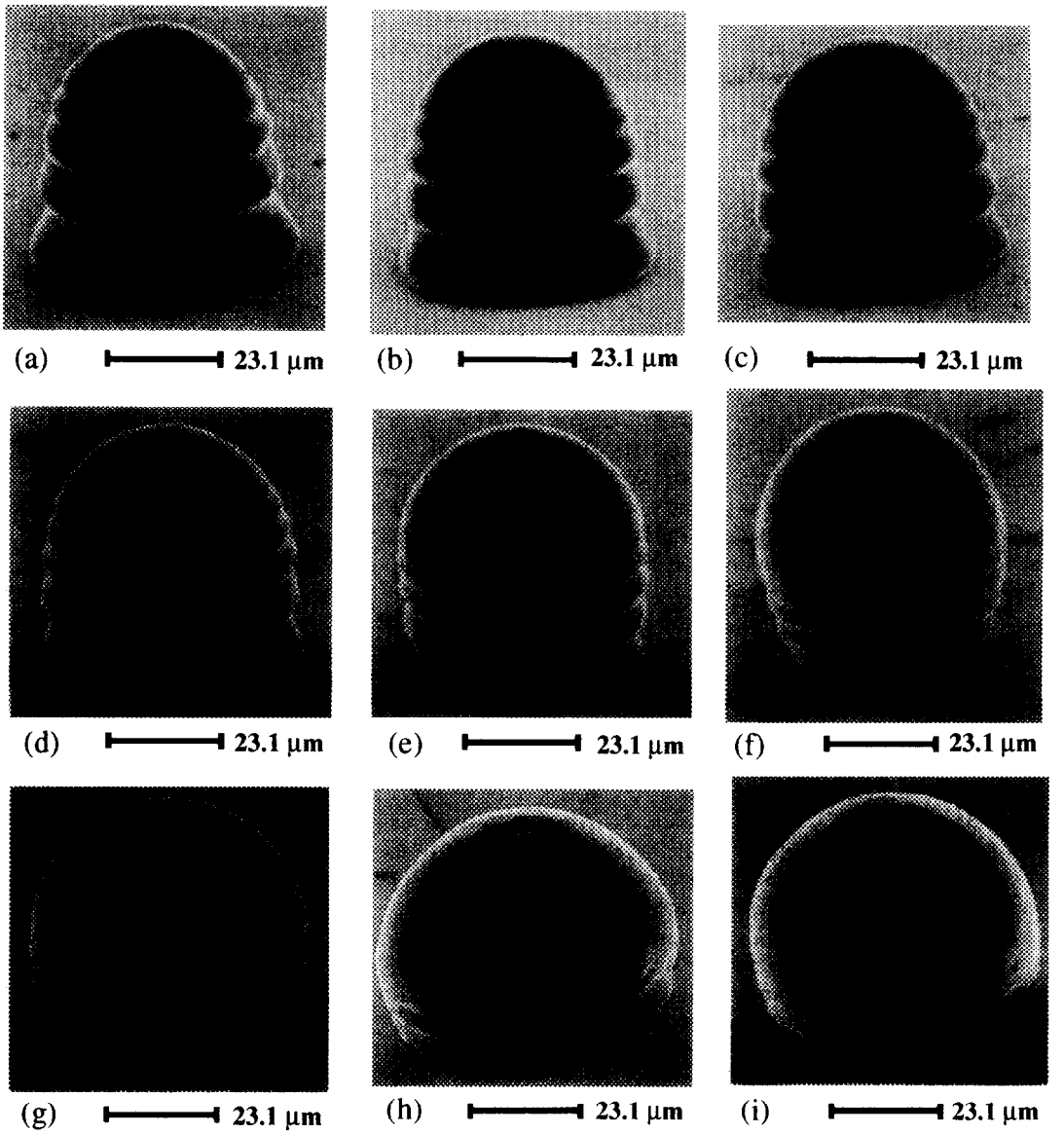

Fig. 10. Scanning electron micrographs of 63% Sn–37% Pb solder droplets deposited on a 0.1 μm Au–2.0 μm Ni–0.3 μm Cu–0.08 μm Cr–678 μm Si substrate at following temperatures, $T_{2,0}$: (a) 35°C; (b) 45°C; (c) 55°C; (d) 65°C; (e) 75°C; (f) 85°C; (g) 95°C; (h) 105°C and (i) 115°C.

in the form of comparisons to a baseline case of typical solder jetting conditions. Variations in the initial droplet temperature, impact velocity, interfacial contact resistance and initial substrate temperature were studied to demonstrate their impact on deposit shapes and on the times to initiate and complete freezing. In many cases, nonintuitive results were observed. For example, within the range of process parameters considered, the solidification time decreased as the initial droplet temperature increased. This behavior was further complicated by the coupling effects of variation of the impact velocity. As the velocity was decreased, the solidification time exhibited an increasingly non-monotonic dependence on the droplet temperature. Also, the effect of variation of the interfacial contact resistance was shown to significantly affect the results. Detailed study of the final solidified shapes, as well as the droplet configuration and flow field at the onset of phase change, illustrated trends with respect to solidification time. For example, as the height of the second deposit surface ripple decreased, the solidification time increased. This behavior was observed for different parameter variation studies, which indicates strong coupling between the droplet dynamics and the freezing behavior.

Scanning electron microscopy was used to analyse 63%Sn–37%Pb solder deposits which were dispensed onto a metallized silicon wafer using a prototype solder jetting apparatus. Qualitatively, features observed in the numerical modelling were also evident in the micrographs. For example, surface ripples are apparent for the lower substrate temperature cases.

The size of and spacing between these ripples on the deposit surface decreases with increasing distance from the substrate. A study of the effect of the substrate temperature on the final droplet shape was also presented. With the aid of theoretical modeling of this process parameter variation, it was possible to explain the physical process responsible for the appearance of a transition in deposit shape which occurred at a particular temperature. The effect of an increase in the substrate temperature was shown to be a delay of the onset of freezing with respect to the droplet oscillation, which led to qualitatively predictable variations in the final solidified shape.

This investigation illustrated the importance of an understanding of the transport phenomena associated with the solidifying droplet impact problem in order to better understand the behavior of the solder jetting process under different operating conditions. The model which was developed and the results it produced should aid in the further development of this novel micromanufacturing approach.

Acknowledgement—The work presented in this paper was supported in part by MicroFab Inc. We thank Dr. David Wallace, Vice President for Technology Development at MicroFab Inc., for his insightful input during the course of the work.

REFERENCES

1. D. J. Hayes, D. B. Wallace and M. T. Boldman, Picoliter solder droplet dispension, *ISHM '92 Proceedings*, pp. 316–321 (1992).
2. F. H. Harlow and J. P. Shannon, The splash of a liquid droplet, *J. Appl. Phys.* **38,** 3855–3866 (1967).
3. F. H. Harlow and J. E. Welch, Numerical calculation of time-dependent viscous incompressible flow of fluid with free surface, *Phys. Fluids* **8,** 2182–2189 (1965).
4. C. S. Fredericksen and A. M. Watts, Finite element method for time-dependent incompressible free surface flow, *J. Comput. Phys.* **39,** 282–304 (1981).
5. E. A. J. Fletcher, *Computational Fluid Dynamics.* Springer, Berlin (1988).
6. G. Trapaga and J. Szekely, Mathematical modelling of the isothermal impingement of liquid droplets in spray processes, *Metall. Trans. B* **22,** 901–914 (1991).
7. K. Tsurutani, M. Yao, J. Senda and H. Fujimoto, Numerical analysis of the deformation process of a droplet impinging upon a wall, *JSME Int. J. Ser. II* **33,** 555–561 (1990).
8. Z. Zhao, D. Poulikakos and J. Fukai, Heat transfer and fluid mechanics during the collision of a liquid droplet on a substrate—I. Modelling, *Int. J. Heat Mass Transfer* **239,** 2771–2789 (1996).
9. J. Fukai, Z. Zhao, D. Poulikakos, C. M. Megaridis and O. Miyatake, Modelling of the deformation of a liquid droplet impinging upon a flat surface, *Phys. Fluids A* **5,** 2588–2599 (1993).
10. Z. Zhao, D. Poulikakos and J. Fukai, Heat transfer and fluid mechanics during the collision of a liquid droplet on a substrate—II. Experiments, *Int. J. Heat Mass Transfer* **39,** 2791–2802 (1996)
11. F. Gao and A. A. Sonin, Precise deposition of molten microdrops: the physics of digital microfabrication, *Proc. R. Soc. Lond. A* **444,** 533–554 (1994).
12. G.-X. Wang and E. F. Matthys, Modelling of heat transfer and solidification during splat cooling: effect of splat thickness and splat–substrate thermal contact, *Int. J. Rapid Solidifi.* **6,** 141–174 (1991).
13. G.-X. Wang and E. F. Matthys, Numerical modelling of phase change and heat transfer during rapid solidification processes: use of control volume integrals with element subdivisions, *Int. J. Heat Mass Transfer* **35,** 141–153 (1992).
14. T. Bennett and D. Poulikakos, Heat transfer aspects of splat-quench solidification: modelling and experiment, *J. Mater. Sci.* **29,** 2025–2039 (1994).
15. P. Bach and O. Hassager, An algorithm for use of the Lagrangian specification in Newtonian fluid mechanics and application to free-surface flow, *J. Fluid Mech.* **152,** 173–190 (1985).
16. C. W. Hirt and B. D. Nichols, Adding limited compressibility to incompressible hydrocodes, *J. Comput. Phys.* **34,** 390–400 (1980).
17. M. Kawahara and H. Hirano, A finite element method for high Reynolds number viscous fluid flow using a two step explicit scheme, *Int. J. Numer. Meth. Fluids* **3,** 137–163 (1983).
18. W. Bushko and I. R. Grosse, New finite element method for multidimensional phase change heat transfer problems, *Numer. Heat Transfer—B* **19,** 31–48 (1991).
19. J. Peraire, M. Vahdati, K. Morgan and O. C. Zienkiewicz, Adaptive remeshing for compressible flow computations, *J. Comput. Phys.* **72,** 449–466 (1987).
20. J. M. Waldvogel, Transport phenomena and solidification in picoliter solder droplet deposition, Ph.D. Thesis, The University of Illinois at Chicago, Chicago (1995).
21. W. Liu, G.-X. Wang and E. F. Matthys, Determination of the thermal contact coefficient for a molten metal droplet impinging on a substrate. In *Transport Phenomena in Materials Processing and Manufacturing*, HTD-Vol. 196, pp. 111–118. ASME, New York (1992).
22. G.-X. Wang and E. F. Matthys, Experimental investigation of interfacial heat transfer for molten metal solidification on a substrate. In *1995 National Heat Transfer Conference—Volume 4* (Edited by R. L. Mahajan), HTD-Vol. 306, pp. 171–179. ASME, New York (1995).